IRAQI JOURNAL OF MATERIALS
Volume (3) Issue (4) October-December 2024, pp. 31-38

Preparation of Highly Pure Nanostructures by Reactive DC Magnetron Sputtering Technique

Firas J. Kadhim [1], Oday A. Hammadi [2], Mohammed K. Khalaf [3]

[1] *Department of Physics, College of Science, University of Baghdad, Baghdad, IRAQ*
[2] *Department of Physics, College of Education, Al-Iraqia University, Baghdad, IRAQ*
[3] *Ministry of Science and Technology, Baghdad, IRAQ*

Abstract
In this work, metal oxide and nitride nanostructures were prepared by reactive dc magnetron sputtering technique. These nanostructures were synthesized from metal oxide such as NiO and nitride such as Si_3N_4 for functional materials applications. The prepared nanostructures were diagnosed by x-ray diffraction (XRD) patterns and Fourier-transform infrared (FTIR) spectroscopy. The results showed that the prepared nanostructures are highly pure, which is ascribed to the featured characteristics of magnetron sputtering technique for such purposes.

Keywords: Magnetron sputtering; Nanostructures; Reactive sputtering; Film growth
Received: 10 April 2024; **Revised:** 12 July 2024; **Accepted:** 19 July 2024; **Published:** 1 October 2024

1. Introduction

Reactive sputtering is a combination of the physical sputtering process and chemical reactions on the target and/or on the substrate in a plasma environment [1]. Because of large number of varying parameters, some simplifications and assumptions have to be done [2]. Using one or two metallic sources in an argon-oxygen (or another reactive gas) ambient for deposition purposes is frequently chosen to increase the flexibility with respect to the chemical compositions that can be accessed [3-6]. Sputtering in an argon-oxygen environment is known as “reactive” magnetron sputtering, where introducing a reactive gas into the sputter system results in the addition of a chemical interaction to the physical process, and therefore compound thin films can be deposited [7-9].

If a reactive gas is added to the sputtering process, it does not only react at the substrate and the chamber walls, but also at the target [10]. At typical working pressures in reactive sputtering (≤0.02mbar), the reaction between the reactive gas and the sputtered atoms that travel towards the substrate in the gas phase cannot occur, because it is impossible to conserve energy and momentum in a two-body collision [11-13]. A surface acts as a third body for reaction, and therefore it is needed for the chemical reaction [14]. Once this reaction happens at the target surface, the sputter process is influenced, as sputter yield and ion-induced secondary electron emission (ISEE) are material-dependent [15].

The sputtering process is entirely influenced by the presence of the reactive gas [16]. Despite that the reactive gas immediately reacts with the metallic particles at the chamber walls, substrate and target, the target condition is not noticeably affected when the flow of reactive gas is relatively low, as the target area is much smaller than the substrate and the compound is sputtered away from the target [17]. Therefore, increasing the flow of the reactive gas causes the total pressure not to increase significantly until a critical flow is reached [18]. At the critical flow, the metallic particles cannot consume all the reactive gas and some amount stays in the gas phase [19]. An increase in reactive gas flow leads to a corresponding increase in the total pressure and the excess of reactive gas may react with the target at the same time [20]. All the ion-target interaction events for argon are also valid for other reactive gases [21].

At the target, the sputter process and compound formation are balanced [22]. A further increase in the reactive gas flow leads, at a given value, to a linear increase in the total pressure [23]. At the target, the compound formation dominates the sputter process. As a result, the sputter rate decreases because the binding energy of the compounds is much higher than that of pure metals [24]. The decrease in sputter rate leads to the availability of a higher concentration of reactive gas molecules,

which turns out in formation of a larger compound area on the target surface, and this is an avalanche [25]. This process is reversible, which supposes that when the flow of the reactive gas is decreased enough, the compound is removed from the target [26]. Because the sputter rate of a compound material is lower than that of the corresponding metallic one, the avalanche happens at lower reactive gas flow [27]. A decrease in discharge voltage in an argon-oxygen environment compared to the discharge voltage in a pure argon environment means an increase of the secondary electron emission yield of the compound when related to the pure metal value [28-32]. The formation of a compound layer in the target surface is called “poisoning” [33]. If the sputter process occurs with the target surface not contaminated (without compound material), it is termed as sputtering in metallic mode [34].

2. Experimental Part

Two types of sputtering targets were used: Nickel sheet of 99% purity for nickel oxide production, while n-type and p-type silicon wafers were used for reactive sputtering experiments using nitrogen gas.

Nickel was selected as a target material because it is readily available material and has good electrical conductivity comparable to copper, gold, silver and platinum. Also, very uniform surfaces of nickel-based films are resulted when deposited on glass substrates due to very good adhesion [35].

Table (1) Physical properties of target materials [36]

Property	Nickel (Ni)	Silicon (Si)
Standard atomic weight	58.6934	28.085
Electron configuration	[Ar] $3d^8$ $4s^2$ [Ar] $3d^9$ $4s^1$	[Ne] $3s^2$ $3p^2$
Density (g/cm^3)	8.908	2.329
Melting point (°C)	1455 °C	1414 °C
Molar heat capacity (J/mol.K)	26.07	19.789
Oxidation state	4, 3, 2, 1, -1	4, 3, 2, 1, -1, -2, -3, -4
Electronegativity	1.91	1.90
Ionization energies (kJ/mol.)	737.1 1753 3395	786.5 1577.1 3231.6
Atomic radius (pm)	124	111
Crystal structure	Face-centered cubic	Diamond cubic
Electrical resistivity (□.m)	$69.3x10^{-9}$	10^3
Thermal conductivity (W/m.K)	99.9	149
Thermal expansion (□m/m.K)	13.4	2.6
Energy band gap	Conductor	1.12 eV

The transparent substrates used in this work were made of borosilicate glass. Before using them for sputtering experiments, they were first cleaned with ethanol to remove any oil layers or residuals may exist on their surfaces, rinsed and washed with distilled water to remove ethanol, and then dried completely before being kept in clean case or placed inside vacuum chamber. Silicon substrates of different conductivities (n-type and p-type) were cleaned by HF acid, ethanol and distilled water, dried and then used for NiO and Si_3N_4 nano films deposition.

The following measurements were carried out on the designed CFUBDM system and NiO and Si_3N_4 samples in order to characterize, classify and optimize them towards the main goal of this work. They include thickness measurements, x-ray diffraction (XRD) pattern and Fourier-transform infrared spectroscopy (FTIR).

The following measurements were carried out on the designed CFUBDM system and NiO and Si_3N_4 samples in order to characterize, classify and optimize them towards the main goal of this work. They include thickness measurements, x-ray diffraction (XRD) pattern, and Fourier-transform infrared spectroscopy (FTIR).

Thickness of the prepared samples was measured by laser-fringes method where two semiconductor lasers of 1mW output power and different wavelengths (532 and 632nm) were used to produce the concentric fringes pattern and hence calculate film thickness (d) from the following relation [37]:

ISSN (print) 2958-8960 (online) xxxx-xxxx Printed in IRAQ

$$d = \frac{L}{\Delta L} \cdot \frac{\lambda}{2} \quad (1)$$

here L and ΔL are the widths of adjacent bright and dark fringes, respectively, and □ is the wavelength of laser beam

Using two wavelengths may make this method reasonably accurate as much as the experimental setup is carefully prepared and stabilized.

The structures of the prepared samples were analyzed with a Bruker D2 PHASER XRD system (Cu-Kα x-ray tube with λ=1.54056Á). A proportional counter of 40 kV and current of 30 mA was used. The XRD patterns were recorded at a scanning rate of 0.08333°s^{-1} in 2□ ranges of 20-60°.

The FTIR measurements were carried out by FTIR spectrometer (SHIMADZU FTIR-8400S) on KBr pellets of the prepared samples.

3. Results and Discussion

The crystallinity of the prepared NiO nanostructures was examined by using powder x-ray diffraction (XRD), as shown in figure (1). Without magnetrons (figure 1a), several peaks belonging to pure nickel appear due to the higher electric power transferred to the discharge volume that generates higher amount of heat inside the chamber. Such heat effect might induce to form these contaminations as the nickel oxide was forming too.

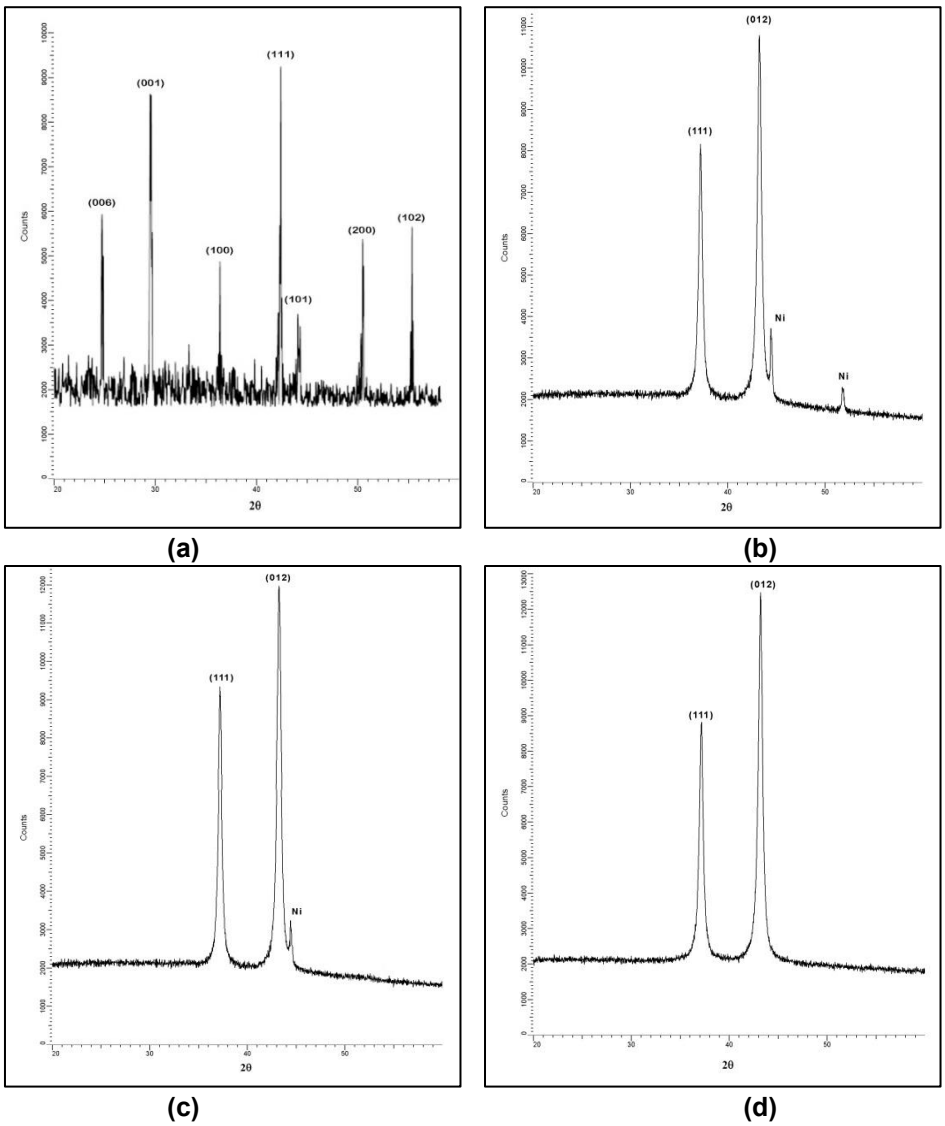

Figure (1) XRD patterns of the prepared NiO samples at different inter-electrode distances (a) 4cm without magnetrons, (b) 2cm, (c) 3cm and (d) 4cm (b-d are with dual magnetrons)

As well, it can be seen that the diffraction peaks are low and broad due to the small size and

incomplete inner structure of the NiO particle. The positions of peaks appearing at 2□ of 37.125° and 43.156° can be readily indexed as (111) and (012) crystal planes of the NiO, as shown in figure (2). Both diffraction peaks can be indexed to the face-centered cubic (f.c.c.) crystalline structure of NiO and corresponding with that of the standard spectrum given by JCPDS 22-1189 [38].

At inter-electrode distance of 2cm, two distinct peaks at 44.45° and 51.8°, belonging to pure nickel, are observed, as shown in figure (1b). This confirms that the majority of sputtered nickel atoms are oxidized before deposited on the substrate and the minority are not oxidized and deposited on the substrate as pure nickel, due to the ferromagnetic property of pure nickel, the sputtered Ni atoms might be accelerated by the intense magnetic field at such distance (2cm), which might prevent them from bonding to oxygen atoms (oxidation).

At inter-electrode distance of 3cm, the peak of pure nickel did not appear as shown in figure (1c). This may be attributed to the excess oxidation of nickel atoms sputtered from the target. Increasing the distance between the electrodes reduces the matching between the magnetic field lines and hence; decreases the magnetic field intensity over the inter-electrode distance. Therefore, the number of sputtered Ni atoms, accelerated by the magnetic field, was accordingly decreased and get a longer time to bond with oxygen atoms to form NiO before deposited on the substrate.

At inter-electrode distance of 4cm, the XRD pattern shows that the samples are single phase and no any other distinct diffraction peaks belonging to pure Ni atoms were detected, as shown in figure (1d). This result shows that the physical phases of the NiO nanostructures, prepared in this work, have higher purity. At such distance, the acceleration effect of magnetic field accelerating sputtered Ni atoms might be disappeared then these atoms would have enough time to be oxidized and deposited as highly pure NiO particles.

The XRD results give an indication that all nickel atoms sputtered from the target are oxidized and then deposited on the substrate as NiO. In table (2), a comparison between experimental x-ray peaks for the NiO samples and standard peaks are presented. The lattice constant and grain size of the NiO nanostructures were calculated from the XRD data and tabulated in table (2). As only two crystal planes were recognized, the average value of the lattice constant can be estimated from them to be 4.04Å with a deviation of about 3% lesser than the standard value (4.17Å). Using Scherer formula, the average grain size can be estimated to be 18.335 nm.

The FTIR spectrum of NiO nanostructures is shown in figure (3), where two bands of significant absorption can be obsered around 410 and 1064.63 cm^{-1}. These bands are attributed to the Ni-O asymmetric and symmetric stretching vibration modes, respectively [39-41]. These broad bands indicate that the structure of NiO include nanocrystals. Three absorption bands at about 1515.94, 1645.17 and 3446.56 cm^{-1} can be attributed to C-O, H-O-H and O-H vibration modes, respectively [42]. Finally, two absorption bands at 3527.56 and 3745 cm^{-1} are observed due to the presence of contaminations, such as nitrogen, hydrogen, carbon dioxide, water vapor [41].

Table (2) Comparison between experimental x-ray peaks for the NiO film and standard peaks

2θ (deg)	d_{hkl} Exp. (Å)	*a* (Å) Exp.	FWHM (deg)	G.S. (nm)	d_{hkl} Std. (Å) [111]	*hkl*	Phase
37.125	2.419	3.42	0.5625	18.83	2.412	(111)	Octahedral
43.156	2.094	4.68	0.59375	17.84	2.088	(012)	Octahedral

The purity and crystallinity of the prepared Si_3N_4 nanostructures were examined by using powder x-ray diffraction (XRD) in the range of 20-60° as shown in figure (4). In figure (4a), a sharp peak belonging to pure silicon is apparently observed and some other peaks belonging to silicon dioxide (SiO_2) are also seen in addition to the formation of Si_3N_4. This may be attributed to the heat generation inside the chamber due to the higher electric power transferred to the discharge volume in absence of magnetrons, whose one of their advantages is the reduction in breakdown voltage as explained before. Therefore, some compounds (e.g., SiO_2) are induced to form at elevated temperatures inside the chamber. Pure silicon atoms appear on the substrate due to the effect of elevated temperature to remove large fraction of the nitrogen (gas) atoms from the discharge region towards cooler regions inside the chamber that prevented them from bonding to sputtered silicon atoms. These results clearly show the advantage of using magnetrons in such technique.

ISSN (print) 2958-8960 (online) xxxx-xxxx Printed in IRAQ

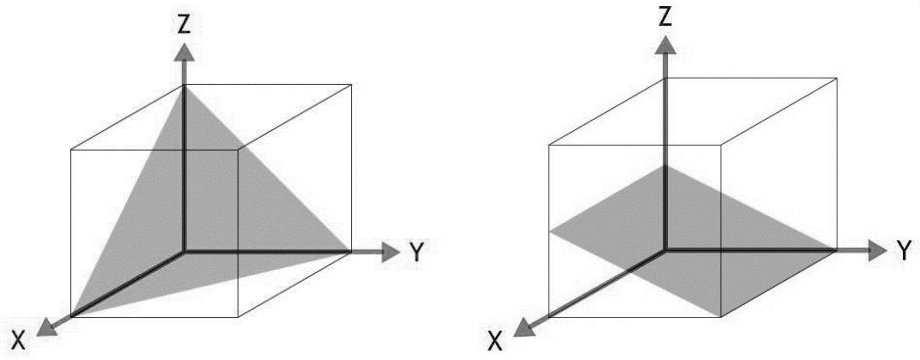

(111) **(012)**

Figure (2) Schematic diagram of the crystal planes formed in NiO nanostructure

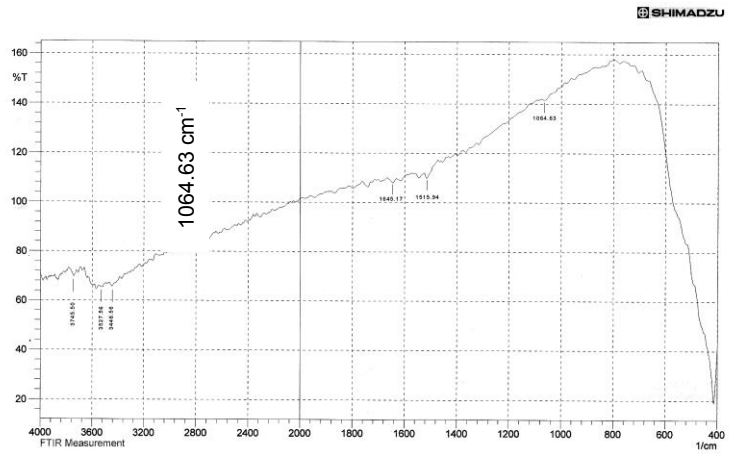

Figure (3) FTIR spectrum of the nickel oxide films prepared at inter-electrode distance of 4cm

The XRD patterns in figures (4b, c and d) explain the formation of nanostructures due to many contributions of crystal planes. At inter-electrode distance of 2cm, a sharp and high peak belonging to pure silicon is seen in addition to many small peaks belonging to nanostructured Si_3N_4. This confirms that a ratio of silicon atoms sputtered from the silicon target was not bonded to nitrogen and then deposited as pure silicon on the substrate. Increasing the inter-electrode distance to 4cm causes the sharp peak of pure silicon to disappear from the XRD pattern and only those peaks belonging to the crystal planes of Si_3N_4 nanostructures are seen. This may be attributed to increasing reaction volume between silicon and nitrogen atoms, therefore, almost all sputtered silicon atoms were bonded to nitrogen atoms to form Si_3N_4 molecules.

The most intense peaks of Si_3N_4 seen on the XRD pattern are (232), (110), (200), (321), (101) and (301) corresponding to diffraction angles of 21°, 23°, 27°, 32°, 36°, and 52°, respectively, and the schematic diagrams of their crystal planes are shown in figure (5). It was not easy to distinguish these peaks individually, as in NiO samples, so, it was very difficult to determine the FWHM values for these peaks and therefore the grain sizes were not determined. However, the average grain size could be precisely determined by the AFM measurements, as shown later. Table (3) includes identification parameters of Si_3N_4 indexed by the JCPDS 29-1132 [43] for hexagonal structure of Si_3N_4. There are many other peaks of lower intensities seen on the XRD pattern but not included in this table.

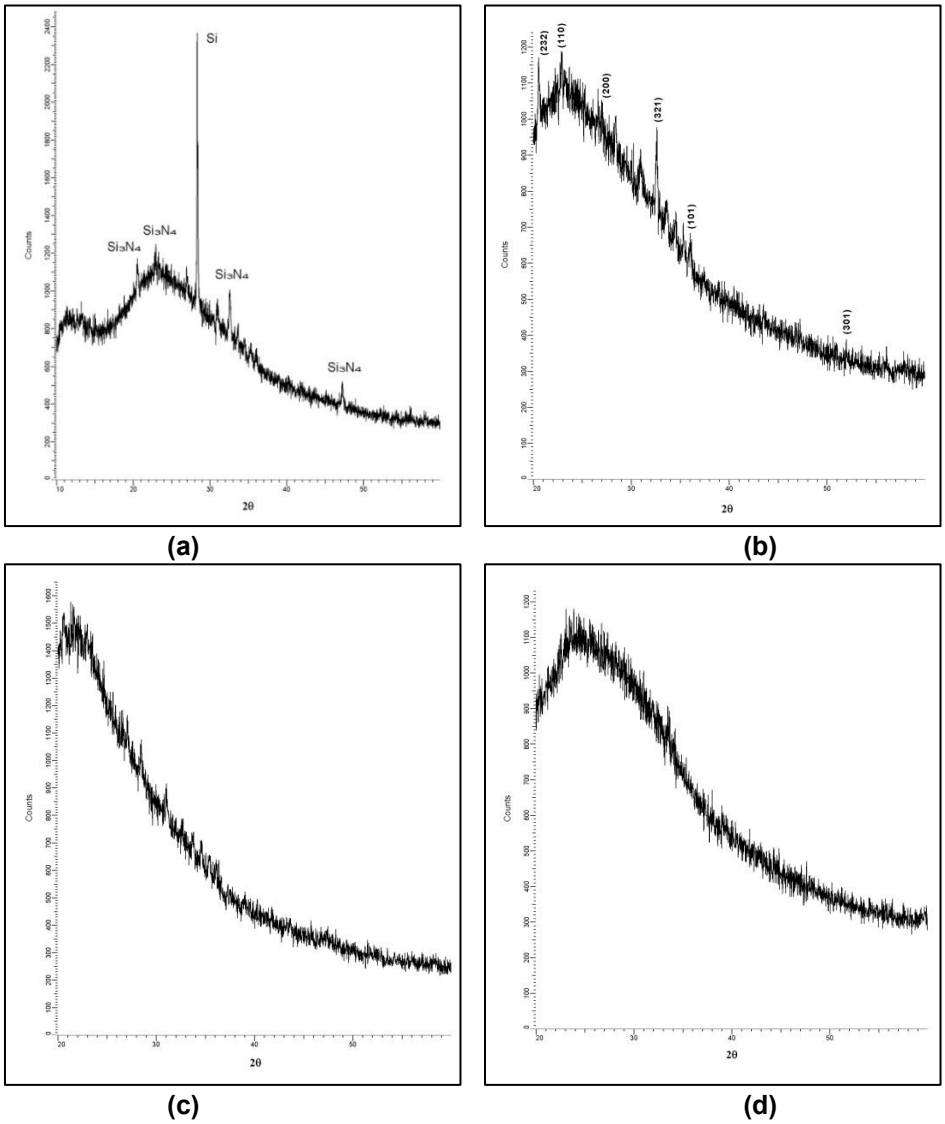

Figure (4) X-ray diffraction patterns of the silicon nitride samples prepared at different inter-electrode distances of (a) 4cm without magnetron(s), (b) 2cm with magnetrons, (c) 4cm with magnetrons and (d) 6cm with magnetrons

Table (3) Identification parameters of silicon nitride obtained from XRD results [117]

2θ (deg)	*d* (Å)	I/I_0	*hkl*	2θ (deg)	*d* (Å)	I/I_0	*hkl*
13.43942	6.58	42	100	41.36508	2.18	33	201
23.38007	3.80	42	110	47.75908	1.902	8	220
27.06844	3.29	100	200	48.02737	1.892	5	211
33.65061	2.66	95	101	49.85031	1.827	12	130
36.0241	2.49	95	210	52.10891	1.753	35	301
38.93992	2.31	6	111	57.8478	1.592	11	221
40.97204	2.20	5	300	59.65571	1.548	6	131

The FTIR spectrum of Si_3N_4 nanostructures is shown in figure (6), where two bands of significant absorption can be seen around 960 and 1086 cm^{-1}. These bands are attributed to the Si-N-Si vibration mode in Si_3N_4 molecule [40]. These broad bands indicates that the structure of Si_3N_4 include nanocrystals.

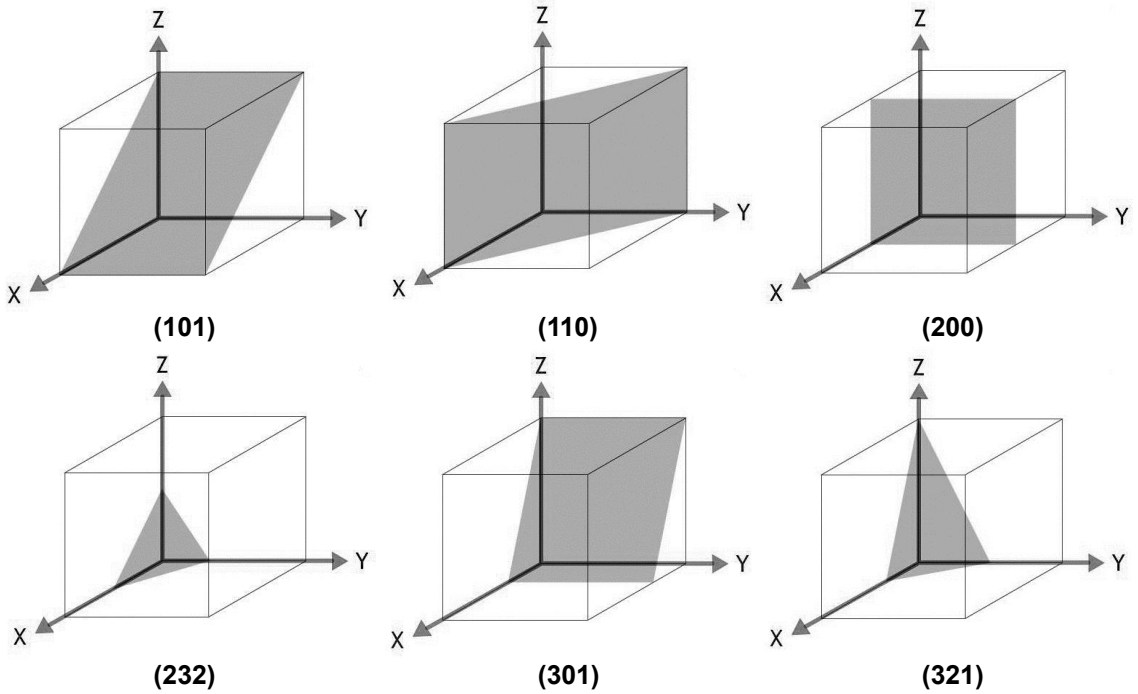

Figure (5) Schematic diagram of some crystal planes formed in the Si_3N_4 samples

The absorption peaks seen around 460 cm^{-1} are attributed to the formation of SiO_2 [42]. Other absorption peaks seen at 1400-3600 cm^{-1} may be attributed to the presence of some contaminations formed on the Si_3N_4 samples when exposed to air. A characteristics feature of silicon nitride is its strong reactivity when exposed to air or humidity, so the surface region of Si_3N_4 film (or powder) has a significant amount of Si_2-NH, Si-NH and Si-OH groups [44].

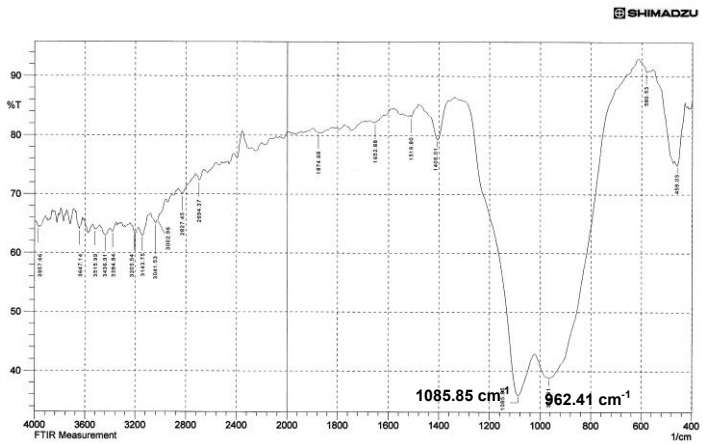

Figure (3-39) FTIR of the Si_3N_4 samples prepared at inter-electrode distance of 4cm

References

[1] M. Ohring, The Materials Science of Thin Films, Academic Press, p. 79, 112 (1992).
[2] D. Huy Trinh, Nanocrystalline Alumina-Zirconia Thin Films Grown by Magnetron Sputtering, Linköping University, Sweden, p. 1 (2008).
[3] K. Wasa, M. Kitabatake, H. Adachi, Thin Film Materials Technology: Sputtering of Compound Materials, William Andrew Inc., p. 139, 116, 2, 119, 72, 106, 103, 9 (2004).
[4] P.M. Martin, Introduction to Surface Engineering and Functionally Engineered Materials, John Wiley & Sons, Inc., p. 339 (2011).
[5] D. Guttler, An Investigation of Target Poisoning during Reactive Magnetron Sputtering, PhD thesis, Technischen Universitat Dresden, p. 3 (2008).
[6] H.B. Nie, Thin Film Deposition and Characterization, National University of Singapore (NUS) (2014).
[7] D. Depla and S. Mahieu, Reactive Sputter Deposition, Springer (2008).

[8] R. Cerc Korošec and P. Bukovec, Sol-Gel Prepared NiO Thin Films for Electrochromic Applications, Acta Chim. Slov., 53, 136-147 (2006).
[9] P.S. Patil and L.D. Kadam, Preparation and characterization of spray pyrolyzed nickel oxide (NiO) thin films, Appl. Surf. Sci., 199, 211–221 (2002).
[10] F.I. Ezema A.B.C Ekwealor and R.U. Osuji, Optical properties of chemical bath deposited nickel oxide (NiO_x) thin films, Superficies y Vacío, 21(1), 6-10 (2008).
[11] A.R. Balu, Nanocrystalline NiO thin films prepared by a low cost simplified spray technique using perfume atomizer, J. Electron Devices, 13, 920-930 (2012).
[12] Yu.G. Dobrovolskiy, V.L. Perevertailo and B.G. Shabashkevich, Anti-reflection coatings based on SnO_2, SiO_2, Si_3N_4 films for photodiodes operating in UV and visible spectral ranges, Semicond. Phys., Quantum Electron. & Optoelectron., 14(3), 298-301 (2011).
[13] X. Zhang and C.P. Grigoropoulos, Thermal conductivity and diffusivity of free-standing silicon nitride thin films, Rev. Sci. Instrum., 66(2), 1115-1120 (1995).
[14] I. Safi, Recent aspects concerning DC reactive magnetron sputtering of thin films: A review, Surf. Coat. Technol., 127, 203-219 (2000).
[15] Wei-Tang Li, Effect of sputtering-gas pressure on properties of silicon nitride films produced by helicon plasma sputtering, Thin Solid Films, 384, 46-52 (2001).
[16] M. Vila, D. Cáceres and C. Prieto, Mechanical properties of sputtered silicon nitride thin films, J. Appl. Phys., 94(12), 7868-7873 (2003).
[17] Gang Xu, Optical investigation of silicon nitride thin films deposited by r.f. magnetron sputtering, Thin Solid Films, 425, 196–202 (2003).
[18] S.A. Awan and R.D. Gould, Conductivity and dielectric properties of silicon nitride thin films prepared by RF magnetron sputtering using nitrogen gas, Thin Solid Films, 423, 267–272 (2003).
[19] I. Levchenko, Stable plasma configurations in a cylindrical magnetron discharge, Appl. Phys. Lett., 85(12), 2202-2204 (2004).
[20] G. Petraconi, Longitudinal Magnetic Field Effect on the Electrical Breakdown in Low Pressure Gases, Brazilian J. of Physics, 34(4B), 1662-1666 (2004).
[21] U.H. Kwon, Multi-scale simulation of plasma generation and film deposition in a circular type DC magnetron sputtering system, Thin Solid Films, 475, 17– 23 (2005).
[22] H.-L. Chen, Y.-M. Lu and W.-S. Hwang, Effect of Film Thickness on Structural and Electrical Properties of Sputter-Deposited Nickel Oxide Films, Materials Transactions, 46(4), 872-879 (2005).
[23] Zh.Q. Yao, Composition, structure and properties of SiNx films fabricated by pulsed reactive closed-field unbalanced magnetron sputtering, Nuclear Instrum. and Methods in Phys. Res., B240, 741–751 (2005).
[24] D. Galvan, Y.T. Pei and J.Th.M. De Hosson, Influence of deposition parameters on the structure and mechanical properties of nanocomposite coatings, Surf. Coat. Technol., 201, 590–598 (2006).
[25] K. Mokeddem, M. Aoucher and T. Smail, Hydrogenated amorphous SiN deposited by DC magnetron sputtering, Superlattices and Microstructures, 40, 598–602 (2006).
[26] Zh.Q. Yao, Studies of the composition, tribology and wetting behavior of silicon nitride films formed by pulsed reactive closed-field unbalanced magnetron sputtering, Nuclear Instrum. and Methods in Phys. Res., B242, 33–36 (2006).
[27] Yu Xiang, Investigation of Ti/TiN multilayered films in a reactive mid-frequency dual-magnetron sputtering, Appl. Surf. Sci., 253, 3705–3711 (2007).
[28] H. Yasuda, L. Ledernez, F. Olcaytug and G. Urban, Electron dynamics of low-pressure deposition plasma, Pure Appl. Chem, 80(9), 1883-1892 (2008).
[29] A. Batan, Characterisation of the silicon nitride thin films deposited by plasma magnetron, Surf. Interface Anal., 40, 754–757 (2008).
[30] M. Awais, Deposition and characterization of NiO_x coatings by magnetron sputtering, Surf. Coat. Technol., 204(16-17), 2729-2739 (2010).
[31] A.A. Turkin, On the evolution of film roughness during magnetron sputtering deposition, J. Appl. Phys., 108, 094330 (2010)
[32] M. Guziewicz, Electrical and optical properties of NiO films deposited by magnetron sputtering, Optica Applicata, XLI(2), 431-440 (2011).
[33] M.A. Signore, Deposition of SiN thin films by RF magnetron sputtering: a material and growth process study, Optical Materials, 34, 632–638 (2012).
[34] Olivier Debieu, Structural and optical characterization of pure Si-rich nitride thin films, Nanoscale Res. Lett., 8, 31, (2013).
[35] Y. Ashok Kumar Reddy, B. Ajitha and P. Sreedhara Reddy, Influence of Growth Temperature on the Properties of DC Reactive Magnetron Sputtered NiO Thin Films, Int. J. of Current Eng. and Technol., Special issue, 351-357 (2014).
[36] Sadik C. Esener, The Future of Data Storage Technologies, Panel report International Technology Research Institute(Maryland, USA), p. 131, 163 (June 1999).
[37] JCPDS 1972, 22-1189, Joint Committee on Powder Standards, Italy (1972).
[38] N.N. Greenwood and E.J.F. Ross, Index of Vibrational Spectra of Inorganic and Organometallic Compounds, vol. I, Butterworth Group (London), p. 326, 328 (1960).
[39] N.N. Greenwood and E.J.F. Ross, Index of Vibrational Spectra of Inorganic and Organometallic Compounds, vol. II, Butterworth Group (London), p. 457 (1963).
[40] N.N. Greenwood and E.J.F. Ross, Index of Vibrational Spectra of Inorganic and Organometallic Compounds, vol. III, Butterworth Group (London), p. 800, 1078 (1966).
[41] Salwan K. Al-Ani, Methods of Determining the Refractive Index of Thin Solid Films, Iraqi J. Appl. Phys., 4(1), 17-23 (2008).
[42] N. Pimpabute, T. Burinprakhon and W. Somkhunthot, Determination of optical constants and thickness of amorphous GaP thin film, Optica Applicata, XLI(1), 257-268 (2011).
[43] JCPDS 1979, C 29-1133, Joint Committee on Powder Standards, International Center for Diffraction Data, USA (1979)
[44] V.P. Tolstoy, I.V. Chernyshova and V.A. Skryshevsky, Handbook of Infrared Spectroscopy of Ultrathin Films, John Wiley & Sons, Inc. (NJ), p. 435 (2003).

 ISSN (print) 2958-8960 (online) xxxx-xxxx Printed in IRAQ